4-2019

A tunable triboelectric wideband energy harvester

Daniel S. Nelson
Binghamton University--SUNY, dnelson7@binghamton.edu

Alwathiqbellah Ibrahim
Binghamton University--SUNY, aibrahi4@binghamton.edu

Shahrzad Towfighian
Binghamton University--SUNY, stowfigh@binghamton.edu

Recommended Citation

Nelson, D., Ibrahim, A., & Towfighian, S. (2019). A tunable triboelectric wideband energy harvester. Journal of Intelligent Material Systems and Structures. https://doi.org/10.1177/1045389X19844012

A Tunable Triboelectric Wideband Energy Harvester

Journal Title
XX(X):1–21

DOI: 10.1177/ToBeAssigned
www.sagepub.com/
SAGE

Daniel Nelson[1], Alwathiqbellah Ibrahim[1], and Shahrzad Towfighian[1]

Abstract

The ability to efficiently convert mechanical energy into electrical energy has become an important topic of discussion and research in the last decade. Triboelectric generators have recently been popular for vibration energy harvesting, but despite plenty of research on its material aspect, research on combining mechanical characteristics and voltage generation output has been sparse. Many energy harvesters suffer from low operating bandwidths and are usually restricted to operating at a specific frequency. We propose a tunable triboelectric energy harvester that has a large response over a wide frequency bandwidth at low frequencies. The tunability is implemented by axially pre-loading a beam that reduces the system stiffness. This stiffness reduction strengthens the collisions that naturally occur in the triboelectric generators, resulting in larger voltage outputs. As the system stiffness decreases, the impacts occur over a broader frequency range, widening the frequency bandwidth. To describe the dynamic and voltage responses, a continuous electromechanical model is derived. The presented mathematical model sheds light on the coupled characteristics of mechanical vibration and triboelectric voltage generation, and can be used as a design tool for high-efficiency energy harvesters to operate wireless sensor networks.

Keywords

Triboelectric, Energy harvesting, wideband frequency, electromechanical model

[1]Binghamton University, 4400 Vestal Parkway E., Binghamton, NY 13902.

Corresponding author:
Shahrzad Towfighian, Binghamton University, 4400 Vestal Parkway E., Binghamton, NY 13902.
Email: stowfigh@binghamton.edu

Prepared using sagej.cls *[Version: 2015/06/09 v1.01]*

Nomenclature	
A_{amp}	Excitation amplitude
A_p	Cross-sectional area of polymer beam
b_m	Width of center mass and upper electrode
B_i, s_i	Constants for mode shape analysis
c, c_i	Mechanical damping coefficient, impact damping coefficient
c_σ	Multiplier for surface charge density
d_0	Initial total electrode gap
D_1	Mechanical damping coefficient for the reduced order model
D_a, D_b	Axial stiffness term, flexural rigidity for second beam span
$D(x)$	Function for flexural rigidity along the beam
E, E_a, E_p	Modulus of elasticity in general, for aluminum, for polymer
E_{air}, E_{PDMS}	Electric fields in the air gap and the PDMS layer
$F(x)$	Function for axial stiffness term along the beam
F_i, F_d	Impact stiffness and damping forces
g, g_i	Acceleration due to gravity, nominal distance between upper electrode and PDMS layer
h, h_m	Thickness of the polymer beam, combined thickness of center mass and upper electrode
I_p	Moment of inertia of polymer beam
k_i, K_L	Impact and linear stiffness coefficients
L, L_1, L_L, L_R	Length of beam, midspan location, location of beginning of upper electrode, location of end of upper electrode
$m(x)$	Function for mass per unit length along the beam
M_1, M_Z	Mass coefficient, base acceleration coefficient
p	Compressive axial force
$q(t)$	Charge transferred through the load resistance
R	Load resistance
S	Contact area
T	Kinetic energy
T_{PDMS}	Thickness of PDMS layer
$u(x,t)$	Longitudinal deflection of the beam
U	Potential energy
$w(x,t)$	Absolute transverse deflection of the beam
W_{nc}	Work done by nonconservative forces
$y(x,t)$	Relative transverse deflection of the beam
$z(t)$	Base motion
z_c	Coordinate for the transverse direction

Introduction

The burgeoning internet of things uses rapidly growing networks of sensors, which urgently need reliable power sources. The major sources for powering sensors are batteries. However, their limited lifespan, detrimental environmental effects, and high replacement costs are significant drawbacks. Mechanical

Nomenclature, cont.	
$\alpha_{a,b}, \beta_{a,b}$	Constants for mode shape analysis
$\alpha_{1,2}$	Electromechanical coupling terms
$\gamma_i(t)$	Arbitrary function of time
δ	Penetration distance
$\varepsilon, \varepsilon_0, \varepsilon_r$	Permittivity, vacuum permittivity, relative permittivity
$\varepsilon_s, \varepsilon_t$	Mechanical strain terms
$\eta(t)$	Function of time
ρ_p	Density of polymer beam
ρ_a	Density of aluminum
ρA	Mass per unit length of second span of beam
σ	Surface charge density
σ_s	Mechanical stress
$\phi(x)$	Mode shape
ω, Ω	Natural frequency, excitation frequency

vibrations are considered one of the most widespread energy sources that can be converted into electrical energy (energy harvesting). These vibrations are prevalent in transportation vehicles, structures, and the environment. The motivation to power small electronics and sensors through harvesting energy from ambient vibrations has driven many research efforts in the last decade (Shafer et al. (2015); Cook-Chennault et al. (2008); Mathúna et al. (2008)). Conventional harvesters maximize the energy they can scavenge when their natural frequency matches the excitation frequency from ambient sources. Because of the narrower bandwidth of the linear harvesters compared to the wider bandwidth of the ambient vibrations, linear energy harvester are considered inefficient. To overcome this limitation, several studies have demonstrated how nonlinear harvesters can attain wider bandwidths than their linear counterparts (Twiefel and Westermann (2013)). The most common types of energy harvesters that can use nonlinearities are magnetic (Ibrahim et al. (2017); Mann and Sims (2009)), mechanical force (Masana and Daqaq (2011a); Sneller et al. (2011)), internal resonance (Chen and Jiang (2015); Yang and Towfighian (2017)), and mechanical stoppers or impacts (Ibrahim et al. (2018); Mahmoud et al. (2009); Soliman et al. (2009)).

When the fundamental frequency of an energy harvester does not match the excitation frequency, even with a small deviation, the harvested energy drops significantly, and the efficiency of the harvester will be low. Accordingly, the need for new energy harvester designs with the capability to tune the resonant frequency has become an important topic. Different research studies addressed this point through closed-loop techniques (Roundy and Zhang (2005); Wu et al. (2006)), or external power sources (Mann and Sims (2009); Shahruz (2006)). One of the most used approaches for frequency tuning is the addition of an axial load, where an axial static load can be applied to the harvester structure to change its natural frequency (Leland and Wright (2006); Morris et al. (2008)). Lesieutre and Davis (Lesieutre and Davis (1997)) found that compressive axial preloads can increase the coupling coefficient of an electrically driven piezoelectric bimorph for a higher output. Leland and Wright (Leland and Wright (2006)) tuned the natural frequencies of a piezoelectric bimorph harvester through applying a compressive axial preload to a

simply supported beam with a center mass. The natural frequencies were reduced by approximately 20%. Roundy and Zhang (Roundy and Zhang (2005)) examined using electrical feedback to tune the resonance frequency of a piezoelectric bimorph. A continuous actuation is needed to adjust the device periodically to tune its resonance frequency. Other ways to tune the bimorph frequency include changing the beam length or the attached mass to control the beam stiffness. Masana and Daqaq (Masana and Daqaq (2011a)) developed and experimentally validated a nonlinear electromechanical model of a clamped-clamped tunable piezoelectric energy harvester subjected to transversal excitations and static axial loading. With the axial load, they were able to achieve a 65% decrease in the natural frequency. Increasing the axial force resulted in higher output energy and bandwidth because of the increase in the electrical damping, oscillation amplitudes, and structural nonlinearity.

In addition to bandwidth, the transduction mechanism used for energy harvesting plays a significant role in energy conversion efficiency. Transducers convert mechanical energy into electrical energy through different mechanisms such as electromagnetic, electrostatic, and piezoelectric (Daqaq (2010); Nguyen et al. (2013); Masana and Daqaq (2011b)). Though piezoelectric generators have been very popular for energy harvesting, their charge density fell behind triboelectric generators (Fan et al. (2012b); Wang (2013)) that were introduced recently for energy harvesting. The area power density of these generators reaches 313 W/m^2 with a conversion efficiency of 60% (Wang (2013)). Triboelectric transduction generates power from the repetitive contact and separation of two materials with different tendencies to lose and gain electrons. Compared with piezoelectric energy harvesters, triboelectric energy harvesters have the advantages of lower fabrication costs, better flexibility, and higher energy density (Wang (2015)). Mechanical impact is an inherent property of the triboelectric generators that can be converted to electricity, but has not received much attention for these generators. In our previous work (Ibrahim et al. (2018)), we showed that the frequency bandwidth widens and higher output can be produced when the triboelectric generators are combined with impact vibration. Although our previous triboelectric impact vibration harvester was effective in increasing bandwidth, the frequency range and further bandwidth widening was fixed by the design of the structure.

To create tunability and to increase output at low frequencies, we introduce the compressive load to the triboelectric energy harvester. The axial force allows the system to be tuned to accommodate various vibration sources at low frequency. The wider frequency bandwidth is achieved because the increase of the axial force reduces the system stiffness, strengthens the collisions between triboelectric layers with small gaps, and spreads the larger output voltage over more frequencies. The result is an energy harvester with its bandwidth widened at low frequencies, which enhances the conversion efficiency because ambient vibrations often have a wide frequency spectrum at low frequencies. Instead of the lumped parameter model used in the previous study, a continuous electromechanical model of the system was developed to accurately capture the dynamic response of the harvester as well as its output. To derive the equations of motion, the Extended Hamilton's Principle for linear Euler-Bernoulli beams and Galerkin's decomposition were used. The model provides a platform for designing high-performance energy harvesters with tunable frequency ranges that are wider spread at low frequencies.

The outline of the article is as follows. The principle of operation will be discussed and a continuous model will be derived in great detail. Experimental results for varying axial forces and excitation amplitudes will be displayed. Then numerical simulations will be performed to show the accuracy of the derived model compared with the experimental results.

Principle of Operation

A solid model and a schematic of the system is shown in Fig. 1. The compressive axial force at the ends of the beam will be tuned to change the system's response and the dynamics. Although a compressive axial force was used in this system, the axial force was controlled so that it was less than the critical axial load. Therefore, the beam will not buckle, but instead, the axial force will reduce the beam's stiffness. The harvester consists of an aluminum upper electrode with semi-cylindrical, 127-micron grooves facing the reversely patterned Polydimethylsiloxane (PDMS) that covers the lower electrode aluminum layer, see Fig. 1c. The two electrodes are connected with a load resistance, and the voltage across the load is measured. When the upper electrode and PDMS layer are initially brought in contact with each other, they will generate triboelectric charges on their surfaces because of the triboelectric effect where the PDMS will be negatively charged and the aluminum will be positively charged. When there is a relative change in displacement between the electrodes, an electric potential difference will be established and charges will be transferred between the electrodes that result in a generated current. When the upper electrode is at its maximum absolute displacement, there will be an equilibrium of charge, and the electric potential difference will be zero. When the two layers approach each other again, the voltage potential difference builds up and causes the current to flow in opposite direction to the previous one. For more details on the operation of triboelectric generators, one can refer to the work conducted by Dr. Z. L. Wang's group (Fan et al. (2012a,b); Wang (2013)).

The system will be subjected to a harmonic base excitation, which will allow the upper and lower electrodes to periodically impact each other at certain frequencies. At frequencies where an impact does not occur, the upper and lower electrodes will effectively behave as a variable capacitor system. An additional mass was placed at the midspan of the beam to increase the inertial force, which will result in a higher velocity and impact force of the upper electrode and a higher voltage output.

Problem Formulation

Mathematical Modeling

We developed a continuous system for the electromechanical governing equations by using linear Euler-Bernoulli beam theory. The continuous system will be more accurate than the model we used for the lumped parameter system previously (Ibrahim et al. (2018)), and it will more easily and accurately capture the effects of the compressive axial force. As the gap will be limited between the upper electrode and the PDMS layer to relatively small distances, any nonlinear effects that would have arisen from mid-plane stretching will be neglected.

To develop the equations of motion, the system is first described. The system will be modeled as a three-span beam, with the first and third spans being the polymer beam, and the second span being a three-layer beam consisting of two aluminum layers and a polymer layer. The system is initially represented in terms of the absolute deflection of the beam and the base motion.

The equations of motion are derived using the Extended Hamilton's Principle. Its kinetic and potential energy terms are written as

$$T = \frac{1}{2}\rho_p A_p \int_0^{L_L} \dot{w}_1^2 dx + \frac{1}{2}\rho A \int_{L_L}^{L_R} \dot{w}_2^2 dx + \frac{1}{2}\rho_p A_p \int_{L_R}^{L} \dot{w}_3^2 dx \tag{1}$$

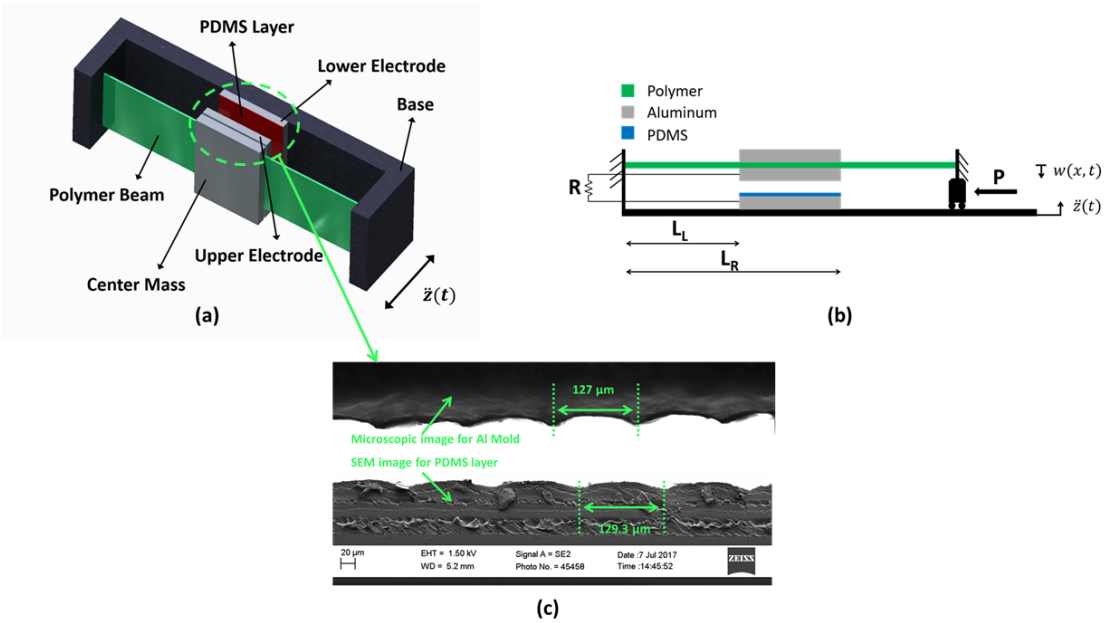

Figure 1. 3D model and schematic of the system. (a) A 3D model of the system. (b) A schematic of the system.(c) Microscopic image of the Al mold and SEM image of the PDMS layer.

where $\rho A = \rho_a b_m h_m + \rho_p A_p$. The potential energy of the system is

$$U = \frac{1}{2}\int_V \varepsilon_{t_i}\sigma_{s_i} d\forall + \frac{\varepsilon_0}{2}\int_V E_{air}^2 d\forall + \frac{\varepsilon_0\varepsilon_r}{2}\int_V E_{PDMS}^2 d\forall \tag{2}$$

where

$$\begin{aligned} \varepsilon_{t_i} &= \varepsilon_{s_i} - z_c w_i'' \\ \varepsilon_{s_i} &= u_i' + \frac{1}{2}w_i'^2 \\ \sigma_{s_i} &= E\varepsilon_{t_i} \\ E_{air} &= \frac{(-q+\sigma S)}{\varepsilon_0 S} \\ E_{PDMS} &= -\frac{q}{\varepsilon_0\varepsilon_r S} \end{aligned} \tag{3}$$

Expanding the potential energy expression using Eq. (3) results in

$$U = \frac{1}{2}E_pA_p\int_0^{L_L}\varepsilon_{s_1}^2dx + \frac{1}{2}E_pI_p\int_0^{L_L}w_1''^2dx + \frac{1}{2}D_a\int_{L_L}^{L_R}\varepsilon_{s_2}^2dx + \frac{1}{2}D_b\int_{L_L}^{L_R}w_2''^2dx$$
$$+ \frac{1}{2}E_pA_p\int_{L_R}^{L}\varepsilon_{s_3}^2dx + \frac{1}{2}E_pI_p\int_{L_R}^{L}w_3''^2dx + \frac{T_{PDMS}}{2\varepsilon_0\varepsilon_rS}q^2 + \frac{d_0 - w_2(L_1) + z(t)}{2\varepsilon_0 S}q^2 \tag{4}$$
$$- \frac{\sigma(d_0 - w_2(L_1) + z(t))}{\varepsilon_0}q + \frac{\sigma^2 S(d_0 - w_2(L_1) + z(t))}{2\varepsilon_0}$$

where

$$\begin{aligned} D_a &= E_ah_mb_m + E_pA_p \\ D_b &= \frac{1}{4}E_ab_m\Big(\frac{h_m^3}{3} + hh_m^2 + h^2h_m\Big) + E_pI_p \end{aligned} \tag{5}$$

The variation of the work from nonconservative forces is

$$\delta W_{nc} = -c\int_0^{L_L}\dot{w}_1\delta w_1dx - c\int_{L_L}^{L_R}\dot{w}_2\delta w_2dx - c\int_{L_R}^{L}\dot{w}_3\delta w_3dx - R\dot{q}\delta q - p\delta w_3(L) \tag{6}$$

Let $w_i(x,t) = y_i(x,t) + z(t)$, and using the Extended Hamilton's Principle $\int_{t_1}^{t_2}(\delta T - \delta U + \delta W_{nc})dt = 0$ yields the governing equations for the longitudinal and transverse directions for each span.

$$\begin{cases} E_pA_p\varepsilon_{s_1}' = 0 & 0 \le x \le L_L \\ E_pI_py_1'''' + \rho_pA_p\ddot{y}_1 + \rho_pA_p\ddot{z} - E_pA_p(\varepsilon_{s_1}y_1')' = 0 & 0 \le x \le L_L \\ \\ D_a\varepsilon_{s_2}' = 0 & L_L \le x \le L_R \\ D_by_2'''' + \rho A\ddot{y}_2 + \rho A\ddot{z} - D_a(\varepsilon_{s_2}y_2')' = 0 & L_L \le x \le L_R \\ \\ E_pA_p\varepsilon_{s_3}' = 0 & L_R \le x \le L \\ E_pI_py_3'''' + \rho_pA_p\ddot{y}_3 + \rho_pA_p\ddot{z} - E_pA_p(\varepsilon_{s_3}y_3')' = 0 & L_R \le x \le L \end{cases} \tag{7}$$

As the mechanical strain is mostly in the longitudinal direction because of limited transverse deflections, the approximation $\varepsilon_{s_i} \approx u_i'$ will be made. The longitudinal and transverse equations of motion will now be decoupled. The boundary conditions will be

$$
\begin{aligned}
u_1(x) &= \gamma_1(t)x + \gamma_2(t) \\
u_2(x) &= \gamma_3(t)(x - L_L) + \gamma_4(t) \\
u_3(x) &= \gamma_5(t)(x - L_R) + \gamma_6(t) \\
u_1(0) &= 0 \\
u_1(L_L) &= u_2(L_L) \\
u_2(L_R) &= u_3(L_R) \\
u_1(L_L) &= -\frac{pL_L}{E_pA_p} \\
u_2(L_R) &= \frac{pL_L}{D_a} - \frac{pL_L}{E_pA_p} - \frac{pL_R}{D_a} \\
u_3(L) &= -\frac{pL}{E_pA_p} + \frac{pL_L}{D_a} - \frac{pL_L}{E_pA_p} - \frac{pL_R}{D_a} + \frac{pL_R}{E_pA_p}
\end{aligned}
\tag{8}
$$

It can be shown that

$$
\begin{aligned}
\varepsilon_{s_1} = \varepsilon_{s_3} &= \gamma_1(t) = \gamma_5(t) = -\frac{p}{E_pA_p} \\
\varepsilon_{s_2} &= \gamma_3(t) = -\frac{p}{D_a}
\end{aligned}
\tag{9}
$$

The longitudinal and transverse equations of motion have now been successfully decoupled. The transverse equations of motion along with the corresponding boundary conditions can now be fully represented. The physical boundary conditions are determined from the clamped edges. Since there is a large plate in the center of the beam, the position at $x = L_L$, and $x = L_R$ is the same, and the slope is zero at $x = L_L$ and $x = L_R$. The remaining boundary condition is determined from the Extended Hamilton's Principle.

$$
\begin{cases}
E_pI_py_1'''' + \rho_pA_p\ddot{y}_1 + \rho_pA_p\ddot{z} + py_1'' = 0 & 0 \le x \le L_L \\
D_by_2'''' + \rho A\ddot{y}_2 + \rho A\ddot{z} + py_2'' = 0 & L_L \le x \le L_R \\
E_pI_py_3'''' + \rho_pA_p\ddot{y}_3 + \rho_pA_p\ddot{z} + py_3'' = 0 & L_R \le x \le L \\
\dot{q} = \frac{-q}{\varepsilon_0 RS}\left[\frac{T_{PDMS}}{\varepsilon_r} + d_0 - y_2(L_1)\right] + \frac{\sigma(d_0 - y_2(L_1))}{\varepsilon_0 R} & \\
y_1(0,t) = 0 & \\
y_1'(0,t) = 0 & \\
y_3(L,t) = 0 & \\
y_3'(L,t) = 0 & \\
y_1(L_L,t) = y_2(L_L,t) & \\
y_2(L_R,t) = y_3(L_R,t) & \\
y_2(L_L,t) = y_2(L_R,t) & \\
y_1'(L_L,t) = 0 & \\
y_2'(L_L,t) = 0 & \\
y_2'(L_R,t) = 0 & \\
y_3'(L_R,t) = 0 & \\
E_pI_py_1'''(L_L,t) + D_by_2'''(L_R,t) - D_by_2'''(L_L,t) & \\
\quad -E_pI_py_3'''(L_R,t) + \frac{q^2}{2\varepsilon_0 S} - \frac{\sigma q}{\varepsilon_0} + \frac{\sigma^2 S}{2\varepsilon_0} = 0 &
\end{cases}
\tag{10}
$$

The mode shapes and natural frequencies of the system around the static configuration will now be determined. The static configuration will be the trivial solution as the transverse motion is perpendicular to the force of gravity. Therefore, there will be a negligible gravitational effect on the static configuration. The deflection about the trivial static configuration is represented as

$$
y_i(x,t) = \phi_i(x)e^{j\omega t} \tag{11}
$$

The i subscript for the mode shape denotes the span, not the mode number, as only the first mode will be considered. Substituting Eq. (11) into Eq. (10) and neglecting the damping, forcing, and electrical terms, yields

$$
\begin{cases}
-\rho_pA_p\omega^2\phi_1 + E_pI_p\phi_1'''' + p\phi_1'' = 0 & 0 \le x \le L_L \\
-\rho A\omega^2\phi_2 + D_b\phi_2'''' + p\phi_2'' = 0 & L_L \le x \le L_R \\
-\rho_pA_p\omega^2\phi_3 + E_pI_p\phi_3'''' + p\phi_3'' = 0 & L_R \le x \le L
\end{cases}
\tag{12}
$$

To simplify, let $\alpha_a = \frac{p}{E_pI_p}$, $\beta_a = \frac{\rho_pA_p\omega^2}{E_pI_p}$, $\alpha_b = \frac{p}{D_b}$, and $\beta_b = \frac{\rho A\omega^2}{D_b}$. Trial functions $\phi_i(x)$ are defined as

$$\begin{aligned}\phi_{1,3}(x) &= B_1\cosh(s_1x) + B_2\sinh(s_1x) + B_3\cos(s_2x) + B_4\sin(s_2x)\\ \phi_2(x) &= B_1\cosh(s_3x) + B_2\sinh(s_3x) + B_3\cos(s_4x) + B_4\sin(s_4x)\end{aligned} \tag{13}$$

where $s_{1,2} = \sqrt{\frac{\mp\alpha_a+\sqrt{\alpha_a^2+4\beta_a}}{2}}$ and $s_{3,4} = \sqrt{\frac{\mp\alpha_b+\sqrt{\alpha_b^2+4\beta_b}}{2}}$. As it is seen in Fig. 2, the mode shape qualitatively describes the physical system, with the polymer beam for the first and third spans and the stiff three layer beam for the second span.

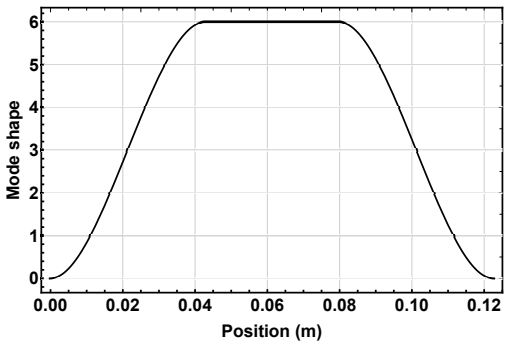

Figure 2. Mode shape of the three span beam with no compressive axial force.

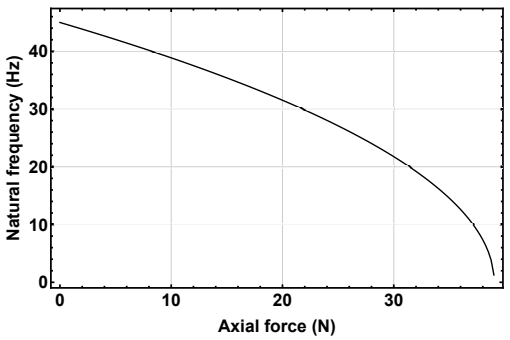

Figure 3. Effect of axial force on the fundamental natural frequency of the system.

The effect of the compressive axial force on the natural frequency is simulated and is shown in Fig. 3. The calculated natural frequency of $45\ Hz$ at zero axial load was in close agreement with a finite element model. This finite element model was created to ensure that for the base case of $p = 0\ N$ the natural frequency matched the analytical value from the mode shape analysis. As the axial force increases before the critical buckling load is reached, the fundamental natural frequency of the system decreases. The natural frequency will theoretically approach zero as the axial force approaches the critical axial load. The critical buckling axial load for this system, as observed in Fig. 3, is approximately $39\ N$.

Reduced Order Model

This section develops a Reduced Order Model to study the dynamics of the system. Now that the mode shape of the system has been determined, the first mode shape of the system will be denoted as $\phi(x)$ and the span notation will not be used anymore. Therefore, the mass per unit length, flexural rigidity, and axial stiffness terms of the system are defined as functions of the longitudinal coordinate.

$$
\begin{aligned}
m(x) &= \begin{cases} \rho_p A_p & 0 \le x \le L_L \\ \rho A & L_L \le x \le L_R \\ \rho_p A_p & L_R \le x \le L \end{cases} \\
D(x) &= \begin{cases} E_p I_p & 0 \le x \le L_L \\ D_b & L_L \le x \le L_R \\ E_p I_p & L_R \le x \le L \end{cases} \\
F(x) &= \begin{cases} E_p A_p & 0 \le x \le L_L \\ D_a & L_L \le x \le L_R \\ E_p A_p & L_R \le x \le L \end{cases}
\end{aligned}
\tag{14}
$$

The Lagrangian of the system $(\mathcal{L} = T - U)$ is constructed and Lagrange's Equations are used to determine the equations for the Reduced Order Model. The substitution $\varepsilon_s = -\frac{p}{F(x)} + \frac{y'^2}{2}$ is used to determine the Reduced Order Model, but the cubic terms can be neglected because of small deformations in the transverse direction of motion. The Lagrangian is defined by

$$
\begin{aligned}
\mathcal{L} = {} & \frac{1}{2} m(x) \int_0^L (\dot{y} + \dot{z})^2 dx - \frac{1}{2} D(x) \int_0^L y''^2 dx - \frac{1}{2} F(x) \int_0^L \Big[- \frac{p}{F(x)} + \frac{1}{2} y'^2 \Big]^2 dx - \frac{T_{PDMS}}{2\varepsilon_0 \varepsilon_r S} q^2 \\
& - \frac{d_0 - y(L_1)}{2\varepsilon_0 S} q^2 + \frac{\sigma (d_0 - y(L_1))}{\varepsilon_0} q - \frac{\sigma^2 S (d_0 - y(L_1))}{2\varepsilon_0}
\end{aligned}
\tag{15}
$$

To approximate the dynamic deflection of the beam about its trivial static configuration, a one mode approximation is used, with

$$
y(x,t) = \phi(x)\eta(t) \tag{16}
$$

By using the one mode approximation and adding the mechanical and electrical damping, a coupled set of ordinary differential equations in $\eta(t)$ and $q(t)$ are generated. After subtracting the static terms, the dynamic coupled equations give

$$
\begin{aligned}
&M_1\ddot{\eta} + M_Z\ddot{z} + D_1\dot{\eta} + K_L\eta + \alpha_1 q^2 + \alpha_2 q = 0 \\
&\dot{q} = -\frac{q}{\varepsilon_0 SR}\left[\frac{T_{PDMS}}{\varepsilon_r} + d_0 - \phi(L_1)\eta\right] + \frac{\sigma(d_0 - \phi(L_1)\eta)}{\varepsilon_0 R}
\end{aligned}
\tag{17}
$$

where

$$
\begin{aligned}
M_1 &= m(x)\int_0^L \phi(x)^2 dx \\
M_Z &= m(x)\int_0^L \phi(x) dx \\
D_1 &= c\int_0^L \phi(x)^2 dx \\
K_L &= D(x)\int_0^L \phi''^2(x) dx - p\int_0^L \phi'^2(x) dx \\
\alpha_1 &= -\frac{\phi(L_1)}{2\varepsilon_0 S} \\
\alpha_2 &= \frac{\sigma\phi(L_1)}{\varepsilon_0} \\
\ddot{z} &= A_{amp}\cos\Omega t
\end{aligned}
\tag{18}
$$

Eq. (18) reveals as the compressive axial force is increased, the linear natural frequency will decrease because of the decreasing stiffness of the system. Therefore, increased axial forces will generate larger responses.

Impact Model

A separate equation of motion must be implemented to describe the case when the impact occurs. When the impact occurs, the upper electrode will penetrate into the PDMS layer, with the maximum penetration distance being δ such that $d_0 = g_i + \delta$. The impact forcing and damping terms are determined by following studies by Narimani et al. (2004); Mahmoud et al. (2009), and letting

$$
\begin{aligned}
F_i &= (K_L + k_i)\eta - k_i g_i \\
F_d &= c_i\dot{\eta}
\end{aligned}
\tag{19}
$$

Once Eq. (19) are substituted into Eq. (17), the full piecewise governing equations are completed. The governing equations for the complete system are shown below. The mechanical equation is represented as a piecewise function, with the condition being whether the upper electrode is separated from the PDMS layer or impacting the PDMS layer.

$$\begin{cases} M_1\ddot{\eta} + M_Z A_{amp}\cos\Omega t + D_1\dot{\eta} + K_L\eta + \alpha_1 q^2 + \alpha_2 q = 0 & y(L_1,t) < g_i \\ M_1\ddot{\eta} + M_Z A_{amp}\cos\Omega t + (D_1 + c_i)\dot{\eta} + (K_L + k_i)\eta - k_i g_i + \alpha_1 q^2 + \alpha_2 q = 0 & y(L_1,t) \geq g_i \end{cases}$$
$$\dot{q} = -\frac{q}{\varepsilon_0 SR}\left[\frac{T_{PDMS}}{\varepsilon_r} + d_0 - \phi(L_1)\eta\right] + \frac{\sigma(d_0 - \phi(L_1)\eta)}{\varepsilon_0 R} \tag{20}$$

Experimental Setup

To experimentally test the concept of the wideband energy harvester, the system was placed on an electrodynamic shaker. Fig. 4 shows the experimental setup. The input signal to the shaker was controlled in a closed-loop with Matlab. The signal was sent to a data acquisition device (NI USB-6251), then through a power amplifier (Techron 5530 Power Supply Amplifier), and then to the shaker. An accelerometer (PCB Piezotronics 352A24) was placed on the base of the shaker and the accelerometer signal was used in the feedback control loop. The accelerometer signal was sent through an amplifier (Kistler Dual Mode Amplifier) and was then sent to the DAQ. The voltage was recorded using an oscilloscope (Tektronix MDO3034). The axial force was controlled by adjusting a screw fixed to the setup. The amplifier that powers the electrodynamic shaker is not pictured. System parameters are defined in Table 1. Trials were conducted in which the compressive axial force and the excitation amplitude were varied and the frequency response of each trial was recorded. The values for the axial force were approximated from the model that produces the corresponding experimentally determined natural frequencies.

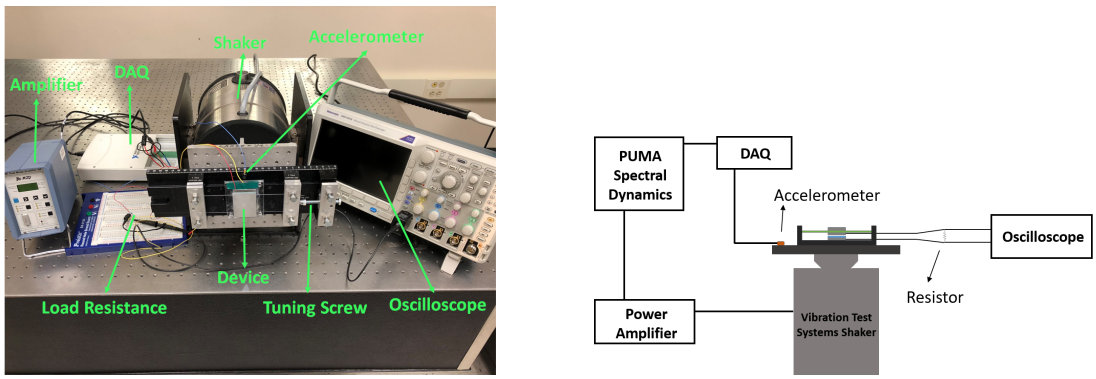

(a) (b)

Figure 4. (a) Picture of the experimental setup, (b) Block diagram of the experimental setup.

Results and Discussions

Experimental frequency response results of various axial forces and acceleration amplitudes are displayed in Figs. 5 and 6. The results show the generator output voltage when the frequencies are swept upward.

Table 1. Experimental parameters

Parameter	Value
$(L$ x b x $h)$	$(12.25$ x 3.7 x $0.1)$ cm
$(L_m$ x b_m x $h_m)$	$(3.7$ x 5.2 x $0.475)$ cm
c	variable
d_0	260 μm
δ	10 μm
g_i	250 μm
E_p	2.344 GPa
R	10 $M\Omega$
T_{PDMS}	500 μm
ε_r	2.5
ρ_p	1220 $^{kg}/_{m^3}$
σ	variable
k_i	2000 $^{N}/_{m}$
c_i	5000 $^{Ns}/_{m}$

Regarding Fig. 5, each set of plots are conducted at a fixed excitation amplitude with a varying axial force. As the axial force was varied, the natural frequency was experimentally recorded and the corresponding axial force was determined through the relationship that is seen in Fig. 3. The larger the axial force, the higher the output voltage. This is because the axial force reduces the system's stiffness. This stiffness reduction allows the upper electrode to travel at faster velocities, which corresponds to a harder impact between the upper electrode and the PDMS layer causing a larger output. The stiffness reduction is shown by the shift of the natural frequency with the change in the axial force. The operating bandwidth increases with the increase in axial force. The bandwidth is measured by recording the frequency difference where the RMS voltage is 0.5 V. With the higher axial force, there is a significant increase in voltage output. Now regarding Fig. 6, each set of plots are conducted at a constant axial force value, with varying excitation amplitudes. With higher excitation amplitudes, there are higher voltage outputs, caused by harder impacts. The operating bandwidth increases with the increase in excitation amplitude, which is due to the impact being able to occur over a larger frequency range. And as the impact is related to more noticeable voltage outputs, larger operating bandwidths are seen. For the low axial force cases, there is a gradual increase in voltage output with excitation amplitude. But with stronger axial forces, the voltage outputs increase at a faster rate with the same excitation amplitude steps. We hypothesize this occurs from a greater increase of the charge density because of the stronger collision as the system's stiffness decreases. The small frequency bump at low frequencies is attributed to the other harmonics of the response.

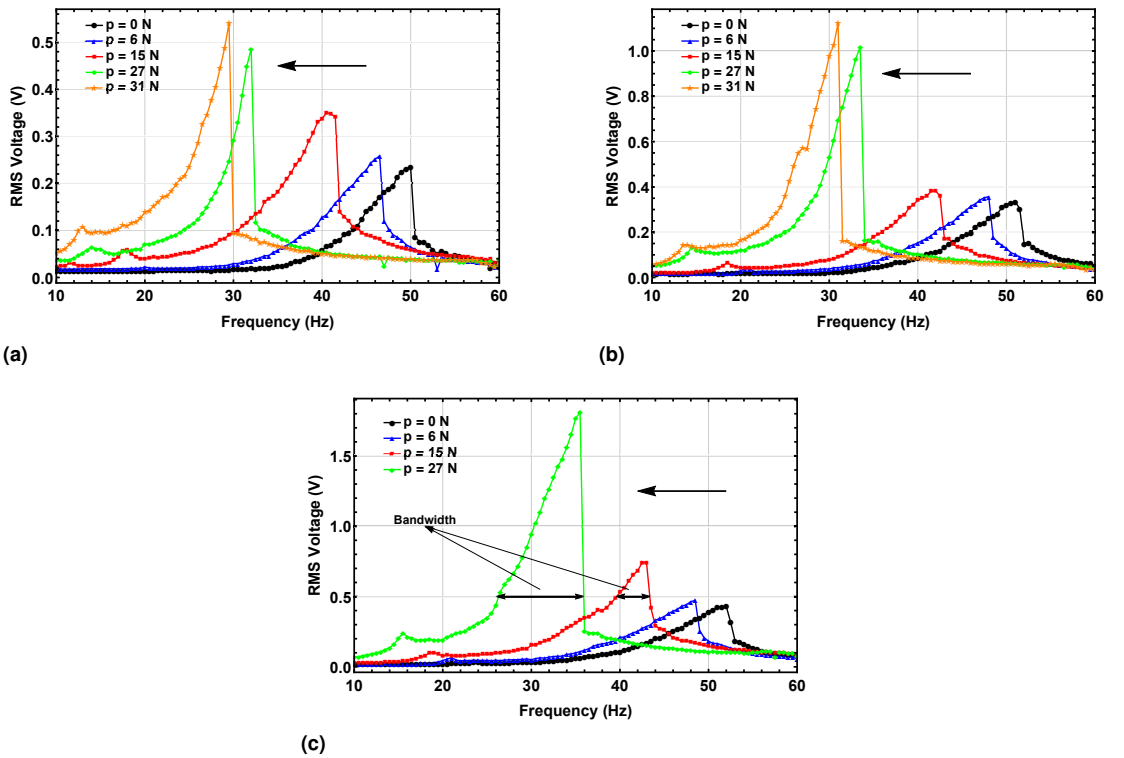

Figure 5. Experimental results for various axial forces and acceleration amplitudes of (a) $0.6g$, (b) $0.8g$, and (c) $1.0g$. The arrow indicates the direction of increasing the axial force.

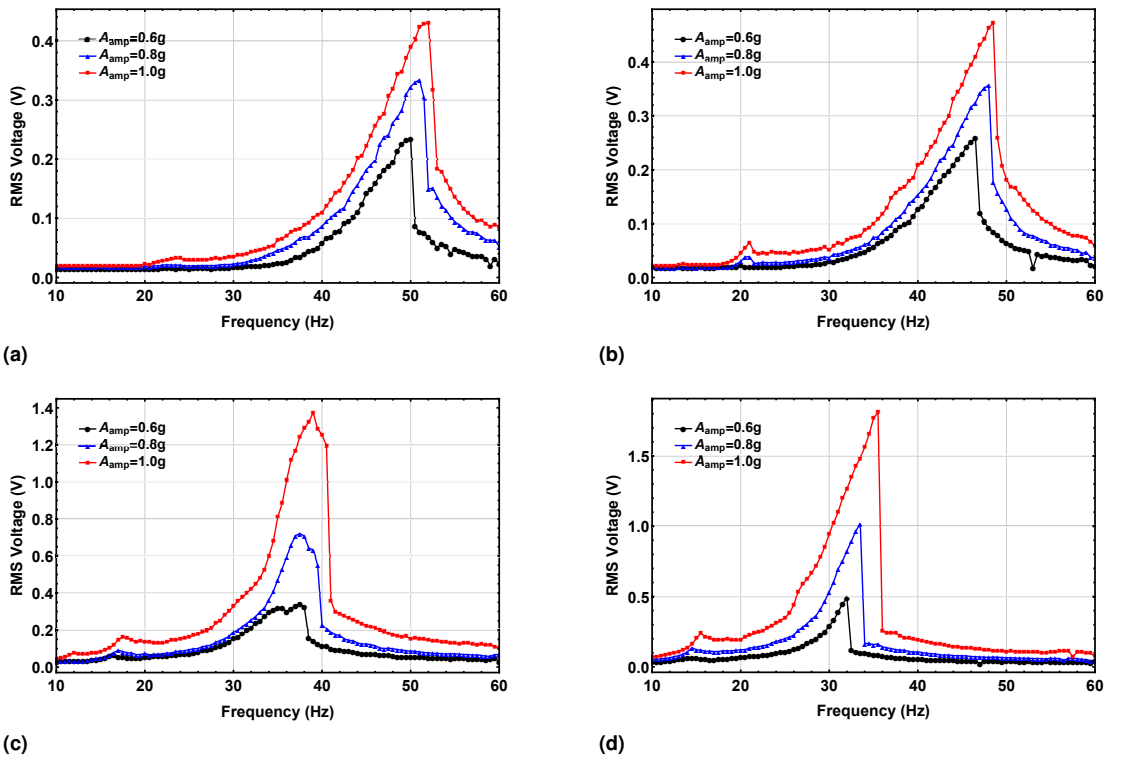

Figure 6. Measured frequency voltage responses for various excitation amplitudes at axial forces of (a) $0.0\ N$, (b) $6.0\ N$, (c) $21.0\ N$, and (d) $27.0\ N$

To validate the reduced order electromechanical model (Eq. (20)), the Shooting Method was implemented to numerically solve for the frequency response of the system. The Shooting Method is a computationally efficient alternative to Long Time Integration as the response is iteratively calculated until the correct initial conditions are determined for periodic solutions (Younis (2011)). First, displacement frequency responses are obtained using the shooting technique. For an axial force of $p = 6\ N$, the maximum displacements at the center are displayed in Fig. 7. In this figure, as expected, the frequency bandwidth widens as the excitation amplitude increases (comparing parts (a) and (b)). The flat region indicates the impact that occurs between the triboelectric layers and that the displacement is limited by the lower electrode at a small distance. Increasing the axial force from $p = 6\ N$ to $p = 15\ N$ widens the frequency bandwidth (see Fig. 8). This widening happens because the stiffness reduction increases the amplitude at the same frequency, and since the travel range is limited, the impact region widens over the frequency range. To shed light on the electromechanical coupling of the system, the voltage frequency responses are then obtained that present useful information about the relationship between axial force, impact, and triboelectric voltage generation.

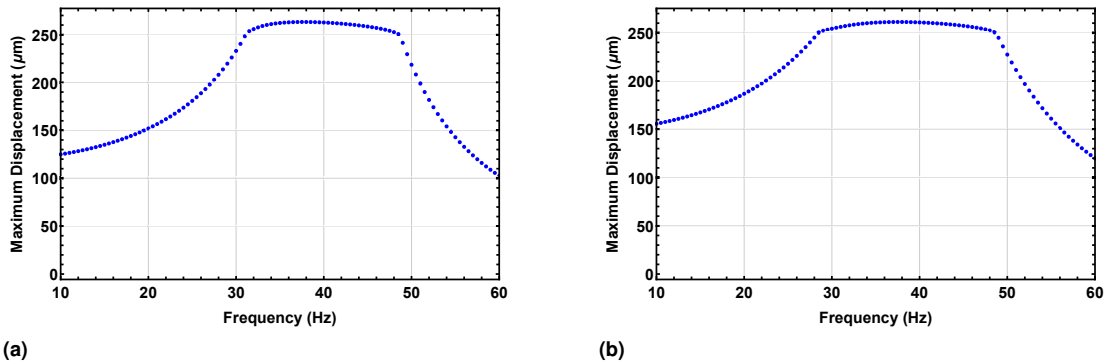

Figure 7. Simulated maximum displacement when (a) $p = 6\ N$ and $A_{amp} = 0.8g$, (b) $p = 6\ N$ and $A_{amp} = 1.0g$

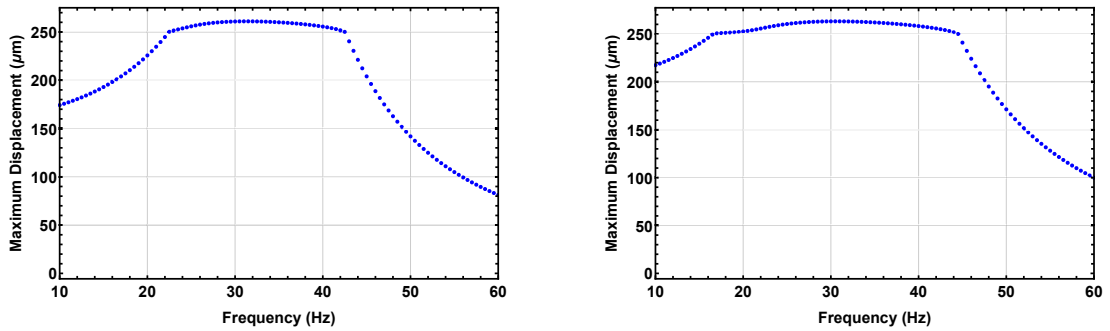

Figure 8. Simulated maximum displacement when (a) $p = 15\ N$ and $A_{amp} = 0.8g$, (b) $p = 15\ N$ and $A_{amp} = 1.0g$

Case studies include voltage frequency responses for three different axial forces, each at two excitation amplitudes, see Figs. 9 to 11. It is noted that the value of the surface charge density is not constant, but varies with the frequency. For the frequency ranges when there is no impact, there is a constant free vibration surface charge density. Once the impact between the upper electrode and PDMS layer starts occurring, the surface charge density increases with the frequency. The increase occurs because, in the impact region, an increase of the frequency causes a harder collision that generates larger penetration into the PDMS layer. The larger penetration produces more charges on the contact surfaces of PDMS and Al that accumulate resulting in higher output voltage as the frequency increases. For the scope of this paper, an empirical recursive model for the surface charge density is determined as $\sigma_i = \sigma_{i-1} \cdot c_\sigma$, where σ is the surface charge density that starts with the free vibration density and c_σ is a multiplier for the surface charge density. The subscript i indicates a frequency step where the impact happens, and $i - 1$ denotes the preceding frequency step. For each trial of axial force, values for the free vibration surface charge density and its multiplier were identified by comparing simulations and experiments. This formula is only used in the impact region, which means it starts at the first frequency where impact occurs and ends at the frequency where impact ends. Further investigation is required for a more accurate dynamic model for the surface charge density, but this simplistic model could explain the drastic increase of the slope in the frequency response as a stronger collision occurs. The mechanical damping coefficients (c) vary by the axial force. The variability is because the support is not perfectly rigid and thus affects the support loss at each axial force. These values are identified from the experiments and are reported in the captions of Figs. 9 to 11. The coefficients for impact damping (c_i) and impact stiffness (k_i) were chosen by first ensuring that an impact and rebound occurred, and then by matching the frequency response of the system during the impact region. These values are reported in Table 1.

As this paper is focused on energy harvesting, power output is also considered. As the output power is related to the voltage and the load resistance, it is necessary to determine the optimal resistance in order to maximize the power output. This is a critical step because in general, tuning the load resistance is one of the easier parameters to tune in a system. The optimal load resistance is obtained by determining the maximum RMS voltage value in the frequency range of $10 - 60\ Hz$ and then varying the load resistance

until the maximum power is found. The calculated average powers based on the RMS voltage values are depicted in Fig. 12. The figure compares average power for two cases of no axial force and an axial force of $p = 15\ N$. As seen in this figure, with larger axial forces, there are higher output power values and higher optimal load resistances. The optimal load resistance for the case of no axial force is around $55 - 60\ M\Omega$ and the optimal load resistance for the case of an axial force of $15\ N$ is around $65 - 70\ M\Omega$. This increase is because of the electromechanical coupling of the system, with the electrical components (load resistances) and mechanical components (axial forces) working with each other to create different systems that have different responses.

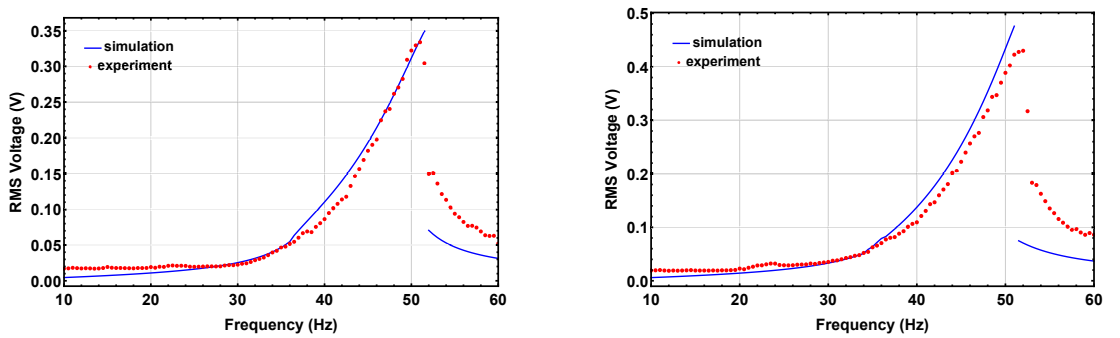

Figure 9. Experimental and simulated voltage frequency response for an expected axial force of $0\ N$, (a) $A_{amp} = 0.8g$, $\sigma = 0.05\ {}^{C}/_{m^2}$, $c_\sigma = 1.05$, $c = 25\ {}^{Ns}/_{m}$ and (b) $A_{amp} = 1.0g$, $\sigma = 0.05\ {}^{C}/_{m^2}$, $c_\sigma = 1.055$, $c = 40\ {}^{Ns}/_{m}$

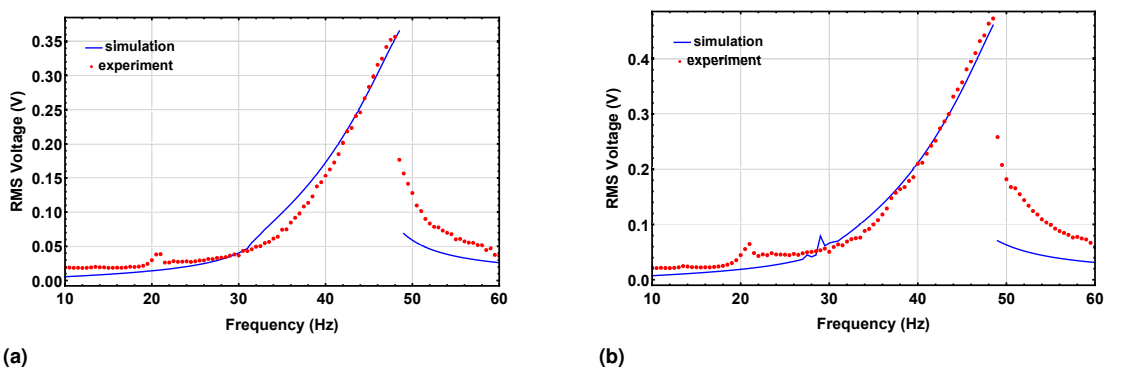

Figure 10. Experimental and simulated voltage frequency response for an expected axial force of $6\ N$, (a) $A_{amp} = 0.8g$, $\sigma = 0.05\ {}^{C}/_{m^2}$, $c_\sigma = 1.047$, $c = 25\ {}^{Ns}/_{m}$ and (b) $A_{amp} = 1.0g$, $\sigma = 0.05\ {}^{C}/_{m^2}$, $c_\sigma = 1.047$, $c = 40\ {}^{Ns}/_{m}$

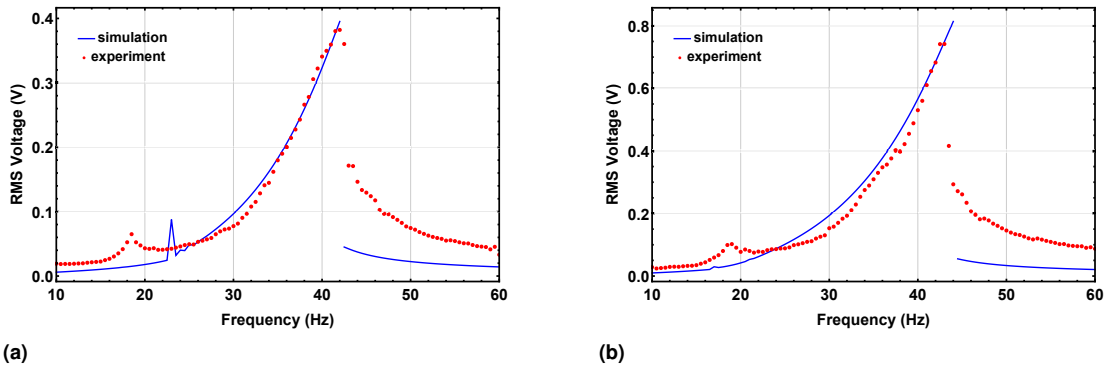

(a) (b)

Figure 11. Experimental and simulated voltage frequency response for an expected axial force of $15\ N$, (a) $A_{amp} = 0.8g$, $\sigma = 0.035\ {}^{C}/_{m^2}$, $c_\sigma = 1.057$, $c = 35\ {}^{Ns}/_{m}$ and (b) $A_{amp} = 1.0g$, $\sigma = 0.041\ {}^{C}/_{m^2}$, $c_\sigma = 1.05$, $c = 40\ {}^{Ns}/_{m}$

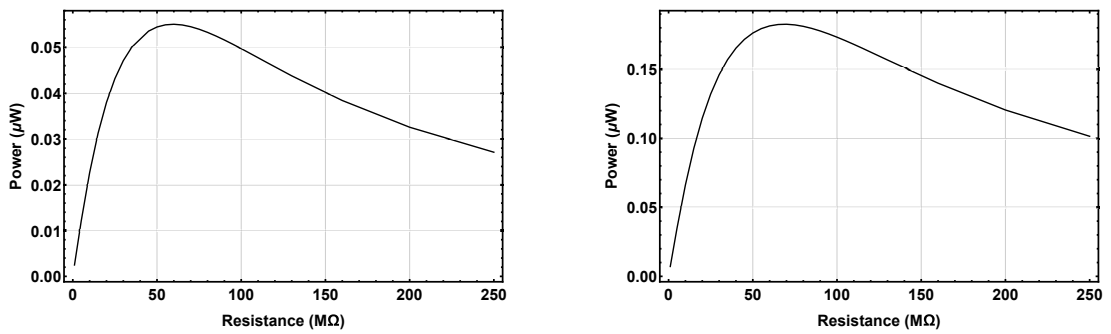

(a) (b)

Figure 12. Average power response curves for various load resistance values and (a) no axial force, (b) axial force of $15\ N$

Conclusions

A tunable wideband energy harvester using triboelectric transduction is introduced to improve efficiency in vibration energy harvesters. The harvester combines the high energy density of triboelectric generators with impact vibration and axial force to enable the use of wider frequency bandwidths at lower frequencies. A continuous electromechanical model was developed that describes the behavior of the system in terms of dynamic amplitudes and voltage outputs. The simulated results were then validated with experimental data. With an increase in the axial force, the voltage output increases. This increase happens because larger collisions occurs between triboelectric layers as a result of the stiffness reduction. The increase in axial force led to an increase in operating bandwidth. The system seemed to behave

differently for weaker and stronger axial forces, with drastic increases in voltage output for stronger axial forces. This increase was explained by the linear increase of the surface charge density as a function of frequency in the impact region. The inclusion of the axial force also allowed the system to be tuned to a wide range of natural frequencies to accommodate different frequency sources. The presented study contributes to the development of triboelectric energy harvesters that can adapt to their environment for powering wireless sensor networks.

References

Chen LQ and Jiang WA (2015) Internal resonance energy harvesting. *Journal of Applied Mechanics* 82(3): 031004–031004–11.

Cook-Chennault K, Thambi N and Sastry A (2008) Powering mems portable devices-a review of non-regenerative and regenerative power supply systems with special emphasis on piezoelectric energy harvesting systems. *Smart Materials and Structures* 17(4): 043001.

Daqaq MF (2010) Response of uni-modal duffing-type harvesters to random forced excitations. *Journal of Sound and Vibration* 329(18): 3621–3631.

Fan FR, Lin L, Zhu G, Wu W, Zhang R and Wang ZL (2012a) Transparent triboelectric nanogenerators and self-powered pressure sensors based on micropatterned plastic films. *Nano Letters* 12(6): 3109–3114.

Fan FR, Tian ZQ and Wang ZL (2012b) Flexible triboelectric generator. *Nano Energy* 1(2): 328–334.

Ibrahim A, Ramini A and Towfighian S (2018) Experimental and theoretical investigation of an impact vibration harvester with triboelectric transduction. *Journal of Sound and Vibration* 416: 111–124.

Ibrahim A, Towfighian S and Younis MI (2017) Dynamics of transition regime in bistable vibration energy harvesters. *Journal of Vibration and Acoustics* 139(5): 051008.

Leland ES and Wright PK (2006) Resonance tuning of piezoelectric vibration energy scavenging generators using compressive axial preload. *Smart Materials and Structures* 15(5): 1413.

Lesieutre GA and Davis CL (1997) Can a coupling coefficient of a piezoelectric device be higher than those of its active material? *Journal of intelligent material systems and structures* 8(10): 859–867.

Mahmoud MAE, Abdel-Rahmany EM, El-Saadany EF and Mansour RR (2009) Battery-less electrostatic micro-power generator. In: *2009 2nd Microsystems and Nanoelectronics Research Conference*. pp. 29–32.

Mann B and Sims N (2009) Energy harvesting from the nonlinear oscillations of magnetic levitation. *Journal of Sound and Vibration* 319(1): 515–530.

Masana R and Daqaq MF (2011a) Electromechanical modeling and nonlinear analysis of axially loaded energy harvesters. *Journal of Vibration and Acoustics* 133(1): 011007.

Masana R and Daqaq MF (2011b) Relative performance of a vibratory energy harvester in mono-and bi-stable potentials. *Journal of Sound and Vibration* 330(24): 6036–6052.

Mathúna CÓ, O′Donnell T, Martinez-Catala RV, Rohan J and O′Flynn B (2008) Energy scavenging for long-term deployable wireless sensor networks. *Talanta* 75(3): 613–623.

Morris DJ, Youngsman JM, Anderson MJ and Bahr DF (2008) A resonant frequency tunable, extensional mode piezoelectric vibration harvesting mechanism. *Smart Materials and Structures* 17(6): 065021.

Narimani A, Golnaraghi ME and Jazar GN (2004) Frequency response of a piecewise linear vibration isolator. *Modal Analysis* 10(12): 1775–1794.

Nguyen SD, Halvorsen E and Paprotny I (2013) Bistable springs for wideband microelectromechanical energy harvesters. *Applied Physics Letters* 102(2): 023904.

Roundy S and Zhang Y (2005) Toward self-tuning adaptive vibration-based microgenerators. In: *Smart Materials, Nano-, and Micro-Smart Systems*. International Society for Optics and Photonics, pp. 373–384.

Shafer MW, MacCurdy R, Shipley JR, Winkler D, Guglielmo CG and Garcia E (2015) The case for energy harvesting on wildlife in flight. *Smart Materials and Structures* 24(2): 025031.

Shahruz S (2006) Design of mechanical band-pass filters for energy scavenging. *Journal of Sound and Vibration* 292(3): 987–998.

Sneller A, Cette P and Mann B (2011) Experimental investigation of a post-buckled piezoelectric beam with an attached central mass used to harvest energy. *Proceedings of the Institution of Mechanical Engineers, Part I: Journal of Systems and Control Engineering* 225(4): 497–509.

Soliman M, Abdel-Rahman E, El-Saadany EF and Mansour RR (2009) A design procedure for wideband micropower generators. *Journal of Microelectromechanical Systems* 18: 1288–1299.

Twiefel J and Westermann H (2013) Survey on broadband techniques for vibration energy harvesting. *Journal of Intelligent Material Systems and Structures* 24(11): 1291–1302.

Wang ZL (2013) Triboelectric nanogenerators as new energy technology for self-powered systems and as active mechanical and chemical sensors. *ACS nano* 7(11): 9533–9557.

Wang ZL (2015) Triboelectric nanogenerators as new energy technology and self-powered sensors–principles, problems and perspectives. *Faraday discussions* 176: 447–458.

Wu WJ, Chen YY, Lee BS, He JJ and Peng YT (2006) Tunable resonant frequency power harvesting devices. In: *Smart Structures and Materials*. International Society for Optics and Photonics, pp. 61690A–61690A.

Yang W and Towfighian S (2017) Internal resonance and low frequency vibration energy harvesting. *Smart Materials and Structures* 26(9): 095008.

Younis M (2011) *MEMS Linear and Nonlinear Statics and Dynamics*. Microsystems. Springer US. ISBN 9781441960207.